The Geometric Effect on the Evolution of a Long Bubble in a Circular Contraction Tube Followed by an Expansion Tube

G.-C. Kuo[a] ,C.-H. Hsu[b], C.-C. Chang[c],Y.-H. Hu[a],
W.-L. Liaw[a] ,K.-J Wang[d], K.-Y. Kung[e,*] , Yute Chen[f]
[a]Department of Mechanical Engineering TIIT
[b]Department of Mechanical Engineering CYCU
[c]Department of Mechanical Engineering, Army Academy R.O.C
[d]Department of Industrial Management
National Taiwan University of Science and Technology
[e,]* Graduate School of Materials Applied Technology
Taoyuan Innovation of Institute Technology
[f]Department of Electronic Engineering, Vanung University
*NO.414, Sec.3, Jhongshan E. Rd., Jhongli City, 32091
Taiwan.
Email:kykoung@tiit.edu.tw, kykoung@gmail.com
Phone: 886-3-4361070-6210, FAX: 886-3-4388198.

Abstract: - In this paper, a long bubble elongates through a contraction tube followed by an expansion tube filled with viscoplastic fluids was studied experimentally and numerically. The effects of both tube geometry and fluid characteristics on the bubble profiles and fractional converge were evaluated.

In the experimental aspect, the bubble profiles and the fractional converge were obtained by image processing the photos captured with a high-speed camera. In the numerical analysis aspect, the continuity equation and momentum equation were converted to the equations in the form of streamline and vorticity. The differential equations were discretized with the finite difference method. Gauss-Seidel Iteration method with successive over-relaxation (SOR) were applied in the computation of the viscous fluid flows. The evolution of the bubble contour predicted by a conservative Level Set Method was applied to this study.

The results showed that the fractional converge of the fluid, the bubble profile and velocity changed due to the effects of the fluid viscosity, the gas the flow rate and the contraction/ expansion angle of the tube. The bubble profile, developing along the stream line, was changed by the effects of the inertia force, surface tension and capillary force, etc. The bubble profiles and the flow fields generated by numerical simulation were applied to explain the experimental observations. Both experimental observation and numerical simulation results were in the same trend. A good consistency was shown between our results and the related researches.

Key-Words: - Evolution, Level Set Method, Long Bubble, Streamline, Viscoplastic Fluids, Vorticity.

1 Introduction

There are many benefits to manufacture the plastic parts by gas-assisted injection molding (GAIM). The parts with better quality are manufactured for uniform pressure distribution throughout the mold by using the nitrogen gas. Therefore, GAIM technique is widely used to manufacture components for automobiles, home appliances, communication products, etc.

A shape profile equation, as the water penetrated the oil in a Hele-Shaw cell, was published by Saffman & Taylor[1] in 1958. The ratio λ was defined as the fraction of the channel was occupied by the bubble. In 1961, Taylor[2] analyzed the fluid deposition in different-sized circular tubes with different fluids. A correlated curve of the fractional coverage to the capillary number was published. In 1980, Pitts[3] reported a theoretical shape equation of the bubble front for $\lambda < 0.77$.

Yamamoto et al.[4] experimentally studied the effect of Capillary number (Ca) and Weiseenberg number (Wi) on capillary number for Newtonian and non- Newtonian fluids.

In 1985, Reinelt and Saffman[5] investigated the fractional coverage and the flow field of viscous fluid by using the finite difference method with composite mesh for both two-dimensional and axisymmetric cases.

In 1987, Song et al.[6] studied the numerical simulation of the flow of upper convected Maxwell fluid through a planar 4:1 contraction by using type dependent difference approximation of the vorticity equation.

In 2010, C. H. Hsu *et.al.*[7] investigated the steady-state flow field of a long bubble penetrating into a region filled with a viscous fluid confined by two closely located parallel plates.The gradually moving of the stagnation point in the front of the bubble tip between two typical flow patterns is clearly presented. In 1997, Huzyak and Koelling[8] studied the influence factors of the fractional coverage for both the Newtonian and viscoelastic fluids experimentally. They showed that the thickness of the coating film was affected by the fluid elasticity of and viscoelastic fluids.

In 2003, Dimakopoulos et al.[9] studied numerically the transient displacement of a viscoplastic material from straight or suddenly constricted cylindrical tubes in 2003. The bubble shapes and contour lines of velocity, the stress tensor and the the pressure field was represented. In 2004, they also studied the transient displacement of viscoelastic fluids by a gas in straight cylindrical tubes[10]. They showed that the thickness of the remaining film was affected by the the viscoelasticity of fluid. The effects of Reynolds number are more pronounced in the case of a viscoelastic than a Newtonian liquid.

In 2007, Dimakopoulos et al.[11] studied the transient displacement of Newtonian and viscoplastic liquids by highly pressurized air in cylindrical tubes of finite length with an expansion followed by a contraction in their cross section. They found that the distribution of the remaining material is affected significantly by the geometry of the tube because the bubble is forced in a very short distance to suddenly expand and then squeeze through the contraction. In 2011, C. H. Hsu *et.al.*[16] investigated a long bubble-driven fluid flow in a circular tube by an optical method. The results showed a good verification of the theoretically derived contour equation. The deduced penetration speed indicated that the speed is increasing downstream caused by the decreasing fluid slug in the tube. The experimental results showed the theoretical bubble profile could be introduced to the simulation study to reduce the calculating time. Dzan *et.al.*[17] applied the digitizing technique of 3D design and experienced the length 9 meters motor skiff and develops precedent of self-reliantly the manufacture motor skiff, also provides fiberglass reinforced plastic of straggling parameter and the improvement direction the vessel 3D design manufacture.

This study analyzed gas penetration through viscoelastic fluids in a contraction/expansion tube. The study parameters in this study are the characteristics of fluid, the flow rate of the injected gas and the contraction/expansion angle. First, the evolution behaviors through viscoelastic fluids of a long bubble in a contraction/expansion tube are recorded by a high speed camera. The profile and speed of the bubble fronts are comapred each other for some different combination of these three parameters.

To explain the experimental observations, a numerical method is also applied to simulate the stable development of long bubbles penetration through viscoelastic fluids in a contraction/expansion tube. By comparing the results of this study and previous researchers, some more reasonable explanations on these complex phenomena can be discussed.

2 Problem Formulation

The behavior of a long bubble through the viscoplastic fluids in a contraction/expansion tube was studied experimentally and numerically in this study. We observe and record the bubble evolution process in a contraction/expansion tube filled with the viscoplastic fluids experimentally.

We also simulate the flow field and the promotion process of a long bubble in a contraction/expansion tube numerically by the finite difference method coupled with the level set method. And then we discuss effects of both tube geometry and fluid characteristics on the bubble profiles and fractional converge according to the results of numerical simulation and those of the experimental observations.

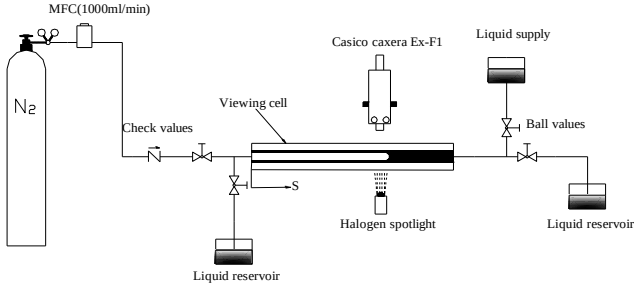

Fig. 1 A schematic diagram of the experimental system.

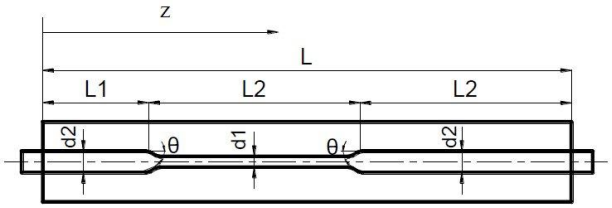

Fig. 2 Schematic of experimental tube.

2.1 Experimental Setup

Fig. 1 shows the experimental setup for the gas penetration. It is designed accoreding the experimental architecture shown by Huzyak et al.[8] in 1997. Some appropriate amendments was applied to make it easy to operate and more suitable to observe and record bubble contours. In this study, the volume rate of injected gas was controlled by using a mass flow controller (MFC).

The images of the bubble are captured by a high-speed camera (CASIO EX-F1) with 6 Mega pixel/60 frames per second. The light source is a coaxial light source (LA180-Me). The pressure at the entrance is 10 kg/cm^2. Nitrogen with 99.99% purity is selected as the injection gas. The volume rate of injection gas was controlled by using a MFC. The gas was injected at two volume rates 600ml/min and 200ml/min.

Fig. 2 shows the experimental tube, which is made of high-hardness heat-resistant glass. The dimensions of the tube are L=1000mm, L1=200mm, L2 =400mm, d2=8mm, d1=4mm. The inclined angle θ are 15° , 45° , 75° and 90° , respectively. The tube was covered by a viewing box dimensions 50mm× 50mm× 1000mm. The viewing cell is filled with glycerin to reduce the experimental errors caused by light refraction. A ruler was fixed to the frame for convenience of calculation of the velocity of the bubble.

2.1.1 Test Fluid

In this study, the viscoelastic fluid carboxymethyl (CMC) with 0.5wt% concentration is used. The definition of Carreau–Yasuda viscosity model[12] is shown as Eq. (1).

$$\mu = \mu_\infty + (\mu_0 - \mu_\infty)(1 + (\lambda \dot{\gamma})^a)^{(n-1)/a} \quad (1)$$

where μ is the measured viscosity, $\dot{\gamma}$ is the applied shear rate, μ_0 is the viscosity limit when $\dot{\gamma} \to 0$, μ_∞ is the viscosity at infinite shear rate, which was set as the solvent viscosity. The parameter λ has units of time, n and a are dimensionless parameters.

The rheological properties tensions of test fluids were measured by a cone-plate type rheometer (Gemini HR nano) at 25℃, which is the same temperature condition for the gas penetration experiments. The parameters of Carreau–Yasuda viscosity model for 0.5 wt% CMC solution are η_0 =0.232 Pas, η_∞ =0.0183 Pas, λ =0.0002 s, a_1=0.1908, a_2=0.1404, $\dot{\gamma}$=0.1/3000.

The surface tension of test fluids with respect to Nitrogen was measured with a Du Nouy (DST30) and the density ρ was measured with a density tester (DA-130N) at 25℃. The density of 0.5 wt% CMC solution is ρ= 945.07 kg/cm^3 and the surface tension σ=0.0733 mN/m.

2.1.2 Experimental method

The experimental procedure of this experiment are summarized as following: The experimental system shown in Fig. 1 are properly mounted on the optical platform. The gas is injected into tube filled with viscolelastic fluids as opening the valve of the inlet side. In order to make bubbles progress stably in the tube, the volume rate of the injection gas was controlled by MFC in this experiment. The profile of the bubble is captured by a high-speed camera.

The photographs captured by the camera are processed by an image post-processor written in Matlab. By using the Level Set Method, the post-processor can apply the binarization and skeletonization treatments to the bubble photographs to eliminate the errors caused by shadows. The bubble profile information is obtained plotted shown as Fig. 5.

2.2 Numerical method

In this study, we simulate a long bubble elongates through a circular tube contraction tube followed by an expansion tube which is filled with viscoplastic fluids numerically.

In the beginning, the tube is filled with viscoplastic fluids. The gas is injected into the tube from the entrance located on the left end of the tube. A long bubble is formed as the gas steadily expels the viscous fluid.

2.2.1 Model Representation

The model schematic drawing of the contraction tube followed by an expansion tube is shown in Fig.3.

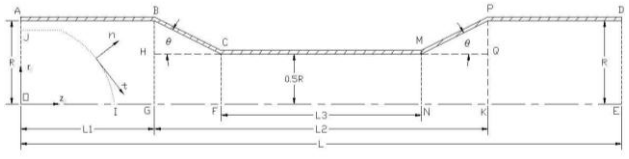

Fig. 3 Schematic of geometric model.

$\overline{OE}$ is the symmetrical axis of the circular tube. The origin of the cylindrical coordinate system is located at O, which is the point center of the entrance cross section. r and z are axis along the radial direction and axis along the axial direction, respectively.

Assume that the angles of the sudden contraction segment $\overline{BC}$ and the sudden expansion segment $\overline{MP}$ are θ. Both the radii of entrance and exit are R which is a constant. The narrowest radius of this contraction tube followed by an expansion tube is 0.5R. The geometry of the flow channel can be defined by the following mathematical equations：

$$r(z)=\begin{cases} R & , z_A \le z \le z_B \\ R-(z-z_B)\tan\theta & , z_B \le z \le z_C \\ 0.5R & , z_C \le z \le z_M \\ 0.5R+(z-z_M)\tan\theta & , z_M \le z \le z_P \\ R & , z_P \le z \le z_D \end{cases} \quad (2)$$

where θ is the constant inclined angle between $\overline{BC}$ (or $\overline{MP}$) with the symmetry axis. $\widehat{IJ}$ is the bubble front profile, i.e. the interface of the gas and fluid. z_A, z_B, z_C, z_D, z_M and z_P are the locations at A, B, C, D, M and P in Fig. 3, respectively.

The fundamental assumptions of the flow are as follows:

1. Incompressible laminar flow, second-grade viscoelastic fluid with finite velocity,
2. Density and other physical properties constant,
3. Fully-developed flow distribution at the entrance,
4. Neumann flow condition ($\frac{\partial}{\partial z}=0$) at the exit,
5. Neglect the weight and buoyancy effects,
6. Axisymmetric problem,
7. No-slip condition on the tube wall.
8. The evolution of the interface is expressed in the conservation form of the level set function

$$\frac{d\phi}{dt}+(\vec{u}\cdot\nabla)\phi=0 \quad (3)$$

Where $\vec{u}=(u_z,u_r)$ is the velocity vector. The function $\phi(r,z,t)$ is defined as $\phi(r,z,t)=0$ for the gas phase, $\phi(r,z,t)=1$ for the liquid phase, and $\phi(r,z,t)=0.5$ for the interface between liquid and gas.

2.2.2 Governing equations

The Rivlin-Ericksen model[13] for a homogeneous, non-Newtonian, second-grade viscoelastic fluid is used in the present flow. The model equation is expressed as follows:

$$\mathbf{T}=-p\mathbf{I}+\mu\mathbf{A_1}+\alpha_1\mathbf{A}_2+\alpha_2\mathbf{A_1}^2 \quad (4)$$

Where $\mathbf{T}$ is stress tensor, p is the pressure, μ is the dynamic viscosity, α_1 and α_2 the first and second normal stress coefficients related to the material modulus. The symbol I is denoted as an identity matrix, and the kinematic tensors $\mathbf{A_1}$ and $\mathbf{A}_2$ are defined as

$$\begin{cases} \mathbf{A_1}=\nabla\cdot\mathbf{V}+(\nabla\cdot\mathbf{V})^T \\ \mathbf{A}_2=\frac{d}{dt}\mathbf{A_1}+\mathbf{A_1}\nabla\cdot\mathbf{V}+(\nabla\cdot\mathbf{V})^T\mathbf{A_1} \end{cases} \quad (5)$$

Where V is the flow velocity vector and d/dt is the material time derivative, b is the conservative body force. Substituted Eq. (4) into the momentum equations

$$\rho\frac{d}{dt}\mathbf{V}=\nabla\mathbf{T}+\rho\mathbf{b} \quad (6)$$

The definitions of Eq.(7) assumed by Rajagopal and Fosdick[14] are used to simplify the equations.

$$\bar{P}=p-\alpha_1\mathbf{V}\cdot\nabla^2\mathbf{V}-\frac{(2\alpha_1+\alpha_2)}{4}|\mathbf{A_1}|^2+\frac{1}{2}\rho|\mathbf{V}|^2+\rho\varphi \quad (7)$$

$$\mu\ge 0\ ,\ \alpha_1\ge 0\ ,\ \alpha_1+\alpha_2=0 \quad (8)$$

Where $\bar{P}$ represent the total force effects. The dimensionless variables are defined as

$$\begin{aligned} &r^*=\frac{r}{R},\ z^*=\frac{z}{R} \\ &u_r^*=\frac{u_r}{U_0},\ u_z^*=\frac{u_z}{U_0} \\ &t^*=\frac{t}{\frac{R}{U_0}},\ p^*=\frac{p}{\frac{\sigma}{R}} \\ &\mathrm{Re}^*=\frac{\rho UR}{\mu} \\ &\omega^*=\frac{\omega}{\frac{U_0}{R}},\ \psi^*=\frac{\psi}{U_0R^2} \\ &E^*=\frac{\alpha_1}{\rho R^2} \end{aligned} \quad (9)$$

where R is the radius of the circular tube, U_0 is the average velocity at the entrance, ρ is the fluid density, μ is the fluid viscosity, σ is the surface tension between the liquid and the gas, Re* is Reynolds number, and E* is the elastic number of the viscoelastic fluid.

The stream function (ψ) and vorticity (ω) are defined as

$$u_r=-\frac{1}{r}\frac{\partial\psi}{\partial z},\ u_z=\frac{1}{r}\frac{\partial\psi}{\partial r} \quad (10)$$

$$\omega=\nabla\times\vec{\mathrm{V}}=-\frac{1}{r}\left(\frac{\partial^2\psi}{\partial r^2}+\frac{\partial^2\psi}{\partial z^2}-\frac{1}{r}\frac{\partial\psi}{\partial r}\right) \quad (11)$$

Substitute dimensionless variables into equations (6) and (11). The dimensionless stream-vorticity equations are obtained after some manipulations.

$$\frac{\partial \omega^*}{\partial t^*}+\frac{\partial^2 \omega^*}{\partial r^{*2}}+\frac{\partial^2 \omega^*}{\partial z^{*2}}+\left(1+\mathrm{Re}^*\frac{\partial \psi^*}{\partial z^*}\right)\frac{1}{r^*}\frac{\partial \omega^*}{\partial r^*}-\mathrm{Re}^*\frac{\partial \psi^*}{\partial r^*}\frac{1}{r^*}\frac{\partial \omega^*}{\partial z^*} \quad (12)$$
$$-\left(1+\mathrm{Re}^*\frac{\partial \psi^*}{\partial z^*}\right)\frac{\omega^*}{r^{*2}}+\mathrm{Re}^* E^* S_0^*=0$$

$$\frac{\partial^2 \psi^*}{\partial r^{*2}}+\frac{\partial^2 \psi^*}{\partial z^{*2}}-\frac{1}{r^*}\frac{\partial \psi^*}{\partial r^*}+r^*\omega^*=0 \quad (13)$$

where S_0^* is the source terms with heigh derivatives.

2.2.3 Numerical scheme

A uniform grid system with grid points $(z_i, r_j) = (z_0 + i\Delta z, r_0 + j\Delta r)$ is applied to the discretized system in this study. The accuracy of stream function (ψ) and vorticity (ω) of the grid system with 193×17, 385×33, 769×65 and 1153×97 grid points are compared each other. After repeated testing, the most appropriate grid resolution is 769× 65 grid points.

The finite difference formulas are obtained from the terms discretized by FDM with SOR method mentioned above. The differential terms of the stream function and the vorticity function are discretized by a second order central difference method. The velocity of grids is calculated from the stream function by a forward difference method. The discretized system could be shown as:

$$\omega_{i,j}^{*K+1}=\frac{\alpha\Delta\tau}{\mathrm{e}}\left(\mathrm{a}\omega_{\mathrm{i+1,j}}^{*K}+\mathrm{b}\omega_{\mathrm{i,j+1}}^{*K}+\mathrm{c}\omega_{\mathrm{i-1,j}}^{*K+1}+\mathrm{d}\omega_{\mathrm{i,j-1}}^{*K+1}+\mathrm{f}\omega_{i,j}^{*K}+\mathrm{g}\right)+(1-\alpha)\omega_{i,j}^{*K} \quad (14)$$

$$\mathrm{a}=\frac{1}{\Delta \mathrm{z}^2}-\mathrm{Re}^*\frac{\partial \psi^{*K}}{\partial r^*}\frac{1}{r|_j}\frac{1}{2\Delta \mathrm{z}}$$

$$\mathrm{b}=\frac{1}{\Delta \mathrm{r}^2}+\left(1+\mathrm{Re}^*\frac{\partial \psi^{*K}}{\partial z^*}\right)\frac{1}{r|_j}\frac{1}{2\Delta r}$$

$$\mathrm{c}=\frac{1}{\Delta \mathrm{z}^2}+\mathrm{Re}^*\frac{\partial \psi^{*K}}{\partial r^*}\frac{1}{r|_j}\frac{1}{2\Delta \mathrm{z}}$$

$$\mathrm{d}=\frac{1}{\Delta \mathrm{r}^2}-\left(1+\mathrm{Re}^*\frac{\partial \psi^{*K}}{\partial z^*}\right)\frac{1}{r|_j}\frac{1}{2\Delta \mathrm{r}}$$

$$\mathrm{e}=\frac{2}{\Delta \mathrm{z}^2}+\frac{2}{\Delta \mathrm{r}^2}+\frac{1}{\left(r|_j\right)^2}$$

$$\mathrm{f}=-\mathrm{Re}^*\frac{\partial \psi^{*K}}{\partial z^*}\frac{1}{r|_j^2}$$

$$\mathrm{g}=\left(\frac{2}{\Delta \mathrm{z}^2}+\frac{2}{\Delta \mathrm{r}^2}+\frac{1}{\left(r|_j\right)^2}\right)\mathrm{Re}^* E S_0^*$$

$$\psi_{i,j}^{*K+1}=\frac{\alpha}{\mathrm{e}_1}\left(\mathrm{a}_1\psi_{i+1,j}^{*K}+\mathrm{b}_1\psi_{i,j+1}^{*K}+\mathrm{c}_1\psi_{i-1,j}^{*K+1}+\mathrm{d}_1\psi_{i,j-1}^{*K+1}+r|_j\,\omega_{i,j}^{*K+1}\right) \quad (15)$$
$$+(1-\alpha)\psi_{i,j}^{*K}$$

$$\mathrm{a}_1=\frac{1}{\Delta \mathrm{z}^2},\ \mathrm{b}_1=\frac{1}{\Delta \mathrm{r}^2}-\frac{1}{2r|_j\,\Delta \mathrm{r}},\ \mathrm{c}_1=\frac{1}{\Delta \mathrm{z}^2},\ \mathrm{d}_1=\frac{1}{\Delta \mathrm{r}^2}+\frac{1}{2r|_j\,\Delta \mathrm{r}}$$

$$\mathrm{e}_1=\frac{1}{\Delta \mathrm{z}^2}+\frac{1}{\Delta \mathrm{r}^2}$$

where α is the over-relaxation factor. k is the iterative index. i and j are the indices along z-direction and r-direction respectively. z and r are the grid sizes along z-direction and r-direction respectively. And $r|_j$ is the j-th grid in r-direction.

The boundary conditions on the surface shown in Fig. 3 are listed as follows:

(a) The surface $\overline{AB}$, $\overline{CM}$ and $\overline{PD}$

$$\omega^*=\frac{2\left(\psi_{\mathrm{i,N}}^*-\psi_{\mathrm{i,N-1}}^*\right)}{r|_j\,\Delta \mathrm{r}^2} \quad (16)$$

(b) The surface $\overline{\mathrm{BC}}$

$$\omega^*=\frac{\psi_{\mathrm{i,j}}^*-\psi_{\mathrm{i-1,j}}^*}{\Delta \mathrm{z}^2}+\frac{\psi_{\mathrm{i,j}}^*-\psi_{\mathrm{i,j-1}}^*}{r|_j\,\Delta \mathrm{r}^2} \quad (17)$$

(c) The surface $\overline{\mathrm{MP}}$

$$\omega^*=\frac{\psi_{\mathrm{i,j}}^*-\psi_{\mathrm{i+1,j}}^*}{\Delta \mathrm{z}^2}+\frac{\psi_{\mathrm{i,j}}^*-\psi_{\mathrm{i,j-1}}^*}{r|_j\,\Delta \mathrm{r}^2} \quad (18)$$

(d) The surface $\overline{\mathrm{DE}}$

$$\omega_{\mathrm{M,j}}^*=\omega_{\mathrm{M-4,j}}^*-2\omega_{\mathrm{M-3,j}}^*+2\omega_{\mathrm{M-1,j}}^*$$
$$\psi_{\mathrm{M,j}}^*=\psi_{\mathrm{M-4,j}}^*-2\psi_{\mathrm{M-3,j}}^*+2\psi_{\mathrm{M-1,j}}^* \quad (19)$$

Equations (14) and (15) could be solved numerically. The value of the over-relaxation factor α is 1.5 for Re*=0. The value of α is adjusted from 0.5 to 0.025 as Re increases from 10 to 400. The values of ω and ψ are calculated iteratively with an over-relaxation factor α until the converge criterion shown as below

$$\left|\frac{\psi_{\mathrm{i,j}}^{*\mathrm{k+1}}-\psi_{\mathrm{i,j}}^{*\mathrm{k}}}{\psi_{\mathrm{i,j}}^{*\mathrm{k}}}\right| \le 10^{-6} \quad (20)$$

2.2.4 Interface tracking scheme

The discretized equation of Eq. (3) with a uniform grid (z_i, r_j) can be written as

$$\frac{\phi_{i,j}^{k+1}-\phi_{i,j}^{k}}{\Delta t}=-\frac{1}{\Delta z}\left(F_{i+\frac{1}{2},j}-F_{i-\frac{1}{2},j}\right)-\frac{1}{\Delta r}\left(G_{i,j+\frac{1}{2}}-G_{i,j-\frac{1}{2}}\right) \quad (21)$$

where Δt is the time step, and $\phi_{i,j}^k$ and $\phi_{i,j}^{k+1}$ are values of $\phi(z_i, r_j)$ at the k-th and (k+1)-th time step, respectively.

The flux on the grid $\phi(z_i, r_j)$ is represented as

$$F_{i+\frac{1}{2},j} = 0.5(\phi_{i,j} + \phi_{i+1,j})u_{z_{i+\frac{1}{2},j}}$$
$$F_{i-\frac{1}{2},j} = 0.5(\phi_{i,j} + \phi_{i-1,j})u_{z_{i-\frac{1}{2},j}} \quad (22)$$

Where $u_{z_{i+\frac{1}{2},j}}$ and $u_{z_{i-\frac{1}{2},j}}$ are the velocity componts on the grid $\phi(z_i, r_j)$.

The normal vector $\mathbf{n}_{i,j}$, curvature $\kappa_{i,j}$ and surface tension $\mathbf{F}_{\mathrm{sa}_{i,j}}$ on the interface [18] can be denoted by

$$\mathbf{n}_{i,j} = \frac{\nabla H_\varepsilon(\phi)}{|\nabla H_\varepsilon(\phi)|} \quad (23)$$

$$\kappa_{i,j} = -\nabla \cdot \left(\frac{\nabla H_\varepsilon(\phi)}{|\nabla H_\varepsilon(\phi)|} \right) \quad (24)$$

$$\mathbf{F}_{\mathrm{sa}_{i,j}} = \sigma \kappa_{i,j} \mathbf{n}_{i,j} \quad (25)$$

where $H_\varepsilon(\phi)$ is the smooth Heaviside function.

$$H_\varepsilon(\phi) = \begin{cases} 0, & \phi < -\varepsilon \\ \frac{1}{2}\left[1 + \frac{\phi}{\varepsilon} + \frac{1}{\pi}\sin\left(\frac{\pi\phi}{\varepsilon}\right)\right], & |\phi| \le \varepsilon \\ 1, & \phi > \varepsilon \end{cases} \quad (26)$$

The parameter ε stands as an effective interface width. The values of ϕ run smoothly from zero to one on the neighboring interface. The values of ϕ may fill up with either 0 or 1 except the neighboring interface, which is treated as a narrow-band in finite terms to assure the high efficiency performance.

An adaptive strategy is applied to determine the values of time step Δt in order to avoid the value of $\varphi_{i,j}$ being less than 0 or greater than 1. The values of $\Delta t \cdot F_{i+\frac{1}{2},j}$, $\Delta t \cdot F_{i-\frac{1}{2},j}$, $\Delta t \cdot G_{i,j+\frac{1}{2}}$, and $\Delta t \cdot G_{i,j+\frac{1}{2}}$ are controlled under the range between 0.2 and 0.4. The values of ϕ are calculated iteratively till the converge criterion in Eq. (27) is reached for some specified tolerance ε_ϕ.

$$\int \left| \phi^{k+1} - \phi^{k} \right| \le \varepsilon_\phi \cdot \Delta t \quad (27)$$

3 Results and discussions

In this study, the behavior of a long bubble through the viscoplastic fluids in a contraction/expansion tube was studied experimentally and numerically. The experimental and numerical results of this study are described below:

3.1 Experimental Results

In this study, the pressure of inlet nitrogen was 10kg/cm^2. Two different nitrogen flow rates controlled by MFC are set as 600ml/min and 200ml/min.

3.1.1 Bubble Profiles

Fig. 4 shows the bubble profile evolution photographs in θ = 45° sudden contraction tube filled with viscoplastic fluid as the gas was injected with the flow rate Q = 200ml/min.

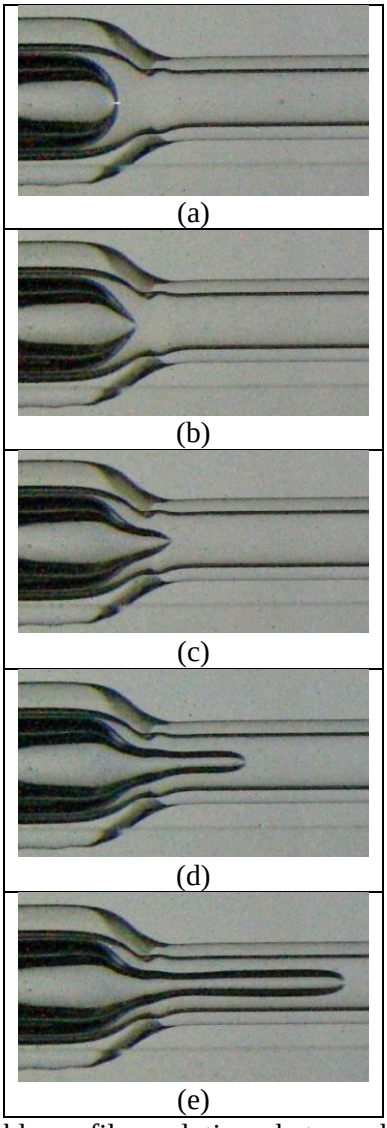

Fig. 4 Bubble profile evolution photographs in θ = 45° sudden contraction tube filled with viscoplastic fluid as Q = 200ml/min.

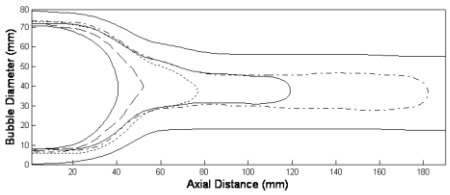

Fig. 5 Overlapping bubble evolution contours.

In order to get a clear observation on the evolution process, the photographs shown in Fig. 4 are processed by an image post-processor written in the Matlab. The overlapping bubble evolution contours shown in Fig. 5 reveals that: The bubble front becomes sharper as it approaches the contraction neck. A well-developed profile appears again after it fully entering the narrower tube. This result is well agreed with the result of Dimakopoulos [9] in 2003.

Dimakopoulos explained this phenomenon that the axial velocity in the liquid is higher the narrower tube and a "elongational" flow field occurs in the entrance of the contraction neck. The capillary forces are rather weak, so that the bubble can penetrate in the narrower tube along with the liquid. However, after entering the tube, it increases its width and its front becomes again nearly parabolic.

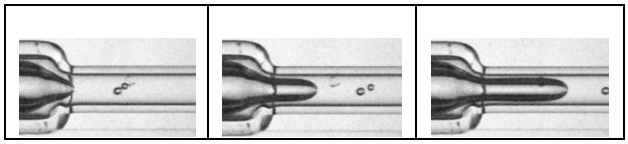

(a) θ =90°，Q=200ml/min

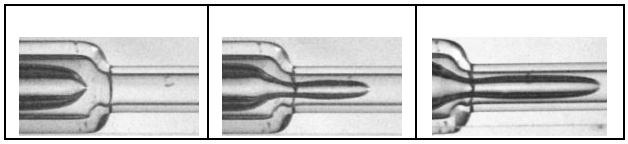

(b) θ =90°，Q=600ml/min

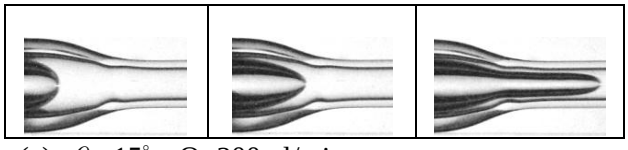

(c) θ =15°，Q=200ml/min

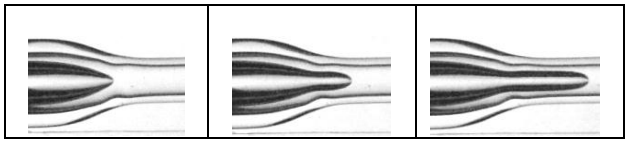

(d) θ =15°，Q=600ml/min

Fig. 6 Bubble profile evolution photographs in sudden contraction tubes filled with CMC 0.5% fluid..

The bubble profile evolution photographs in the θ =90° sudden contraction tube filled with CMC0.5% fluid are shown in Fig. 6 (a) and (b). The gas flow rates are 200ml/min and 600ml/min, respectively. The bubbles front contours shown in Fig 6(b) have an apparent "necking". The bubble front elongates longer and becomes sharper when it entering the contraction region by increasing the flow rate of the injected gas.

The bubble profile evolution photographs in the θ =15° sudden contraction tube are shown in Fig. 6 (c) and (d). The gas flow rates are 200ml/min and 600ml/min, respectively. The bubble profiles in the θ =15° sudden contraction tube are more smooth than those in the θ =90° sudden contraction tube.

Dimakopoulos[15] explained that the inertia forces have a greater impact on the shape of the bubble and the width of the rigid region ahead of bubble tip than the yield stress of the material in a straight geometry.

The bubble contour expanses when the bubble entering the constriction tube, because the effect of capillary forces in the tube.

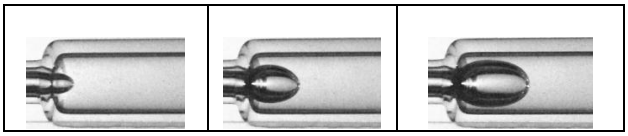

(a) θ =90°，Q=200ml/min

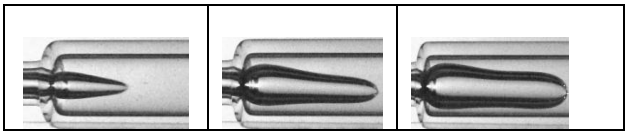

(b) θ =90°，Q=600ml/min

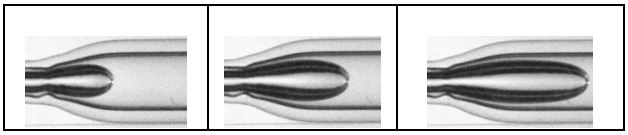

(c) θ =15°，Q=200ml/min

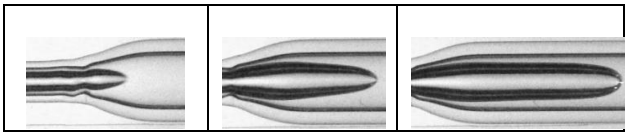

(d) θ =15°，Q=600ml/min

Fig. 7 Bubble profile evolution photographs in sudden expansion tubes filled with CMC 0.5% fluid.

The bubble profile evolution photographs in the θ =90° sudden expansion tube filled with CMC0.5% fluid are shown in Fig. 7(a) and (b). The gas flow rates are 200ml/min and 600ml/min, respectively.

The bubble profile is close to an ellipse with stable and symmetrical shape as the flow rate of injection gas Q=200ml/min. However, the shape of the bubble profile gets longer and sharper with some unstable and asymmetric behaviour as the flow rate of injection gas Q=600ml/min. A more speedy, narrow and sharp bubble contour is formed in the tube by increasing the injected gas flow rate. Due to the changes of fluid viscoelasticity and expansion angle, the transmission differences of the velocity field and pressure field may leads to the instability of the flow field.

Fig. 7(c) and (d) show the bubble profile evolution photographs in the θ =15° sudden expansion tube filled with CMC0.5% fluid. Similar to Fig. 7 (a), the bubble profile is close to an ellipse with stable and symmetrical shape as the flow rate of injection gas Q=200ml/min. The bubble profile gets longer and sharper with a stable and symmetrical shape by increasing the flow rate of injection gas till Q=600ml/min.

In 1980, Pitts showed that when the bubble velocity increases, the ratio of bubble diameter to the tube diameter will decrease monotonously to 0.5. However, Kamisli et al. considered the impact of bubble velocity as well as surface tension on the shape of the bubbles in 2006.

Dimakopoulos explained in 2007 that due to the development of 'lip' or 'corner' vortices and small Reynolds numbers on the expanding side of the tube, the bubble extended distortions on the free surface near the expansion corner.

As the bubble front passing through the expansion corner, it is affected by the inertia force and the surface tension. As the inertia force caused by the velocity of injected gas is more significant, the bubble profile elongates along the flow line, resulting in the development of the slender bubble profile. In other hands, as the surface tension caused by the interface of the gas and the viscoelastic fluid is more significant, it expanses radially to form an ellipse-like profile.

3.1.2 Velocity of Bubble Front

The velocity of bubble front penetrating through CMC0.5% fluid in θ =15° , 45° and 90° sudden contraction/expansion tubes are shown in Fig. 8.

A common trend of the velocity development in the sudden contraction/expansion tubes is described as below: The bubble front accelerates from the contraction neck (z=20 cm) to the position of highest velocity (z=45 cm). Subsequently, the bubble is decelerated till a velocity which is slightly larger than the exit velocity as the bubble front reaches the sudden expansion corner (z=60 cm).

For different incident gas flow rates (Q), the bubble front velocities under Q = 600 mL / min is significantly higher than those under Q = 200 mL / min. Fig. 8 also shows that the bubble front velocity inreases by increasing the sudden contraction / expansion angle (θ) under the same incident gas flow rate.

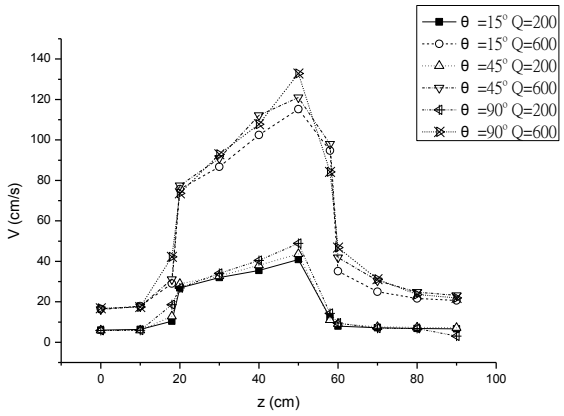

Fig. 8 Velocity of Bubble Front in sudden contraction/expansion tubes filled with CMC0.5% fluid.

3.1.3 Fractional converge

In this paper, the fractional converge (m) of the liquid is estimated by $\frac{R_o^2-R_b^2}{R_o^2}$. Where R_b is the radius of bubble and R_o is the radius of inner tube. The radius of bubble R_b is measured at $1.5R_o$ downstream away from the bubble tip according to the result suggested by Cox showed in 1962.

The fractional converges in θ =15°, 45° and 90° sudden contraction/expansion tubes filled with CMC0.5% fluid are shown in Fig. 9. A common trend for incident gas flow rate Q=600 ml/min is described as below: (1) In the interval 10 cm<z<20 cm, as the bubble front approaching the contraction neck, the fractional converge (m) increases rapidly. (2) In the interval 20 cm<z<50 cm, as the bubble front fully entering the contraction tube, m also increses. (3) In the interval 50 cm<z<60 cm, as the bubble front approaching the, m deceases rapidly. (4) In the interval 60 cm<z<90 cm, as the bubble front

entering fully the expansion tube, m almost keeps a constant value.

Fig.6(b) shows a slender bubble profile which is away from the tube wall farther at the contraction neck in θ =90° sudden contraction/expansion tubes for Q=600 ml/min. Therefore, the fractional converge of the fluid in the wall is larger.

The fractional converge of fluid changes depending on the effect of the viscosity of the fluid, the incident gas flow rate and the contraction / expansion angle.

The fractional converge of fluid increases as the sudden contraction/expansion angle or the injection gas flow rate increases.

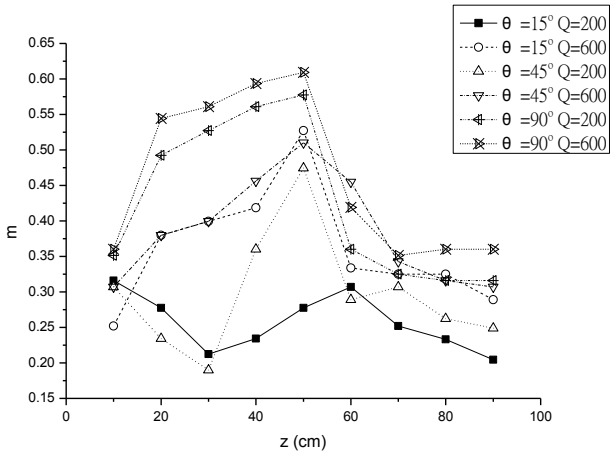

Fig. 9 Fractional converges in θ =15°, 45° and 90° sudden contraction/expansion tubes filled with CMC0.5% fluid.

Dimakopoulos et al.[15] in 2007 described that the distribution of the remaining film on the inner tube wall is non-uniform and only partly follows the tube geometry: it is thinner in the expanding section of the tube, thicker in the contracting one. And they declared that the remaining film thickness depends on liquid inertia and yield stress.

The fractional converge of fluid changes depending on the effect of the viscosity of the fluid, the incident gas flow rate and the contraction / expansion angle.

Under a constant incident gas flow rate, the bubble front velocity increases by increasing the contraction/expansion angle. This will lead to the decreasing diameter of the bubbles as well as the increasing fractional converges of fluid.

The bubble front velocity increases by increasing the incident gas flow. This will also lead to the decreasing diameter of the bubbles as well as the increasing fractional converges of fluid.

3.2 Numerical method

The bubble profiles and the flow fields generated by numerical simulation were applied to explain the experimental observations.

3.2.1 Flow Field

Fig. 10 shows the flow fields of sudden contraction/expansion tube by numerical simulation. Due to the assumption of axial symmetry, the stream function is plotted above the z-axis. The vortiity is plotted under the z-axis.

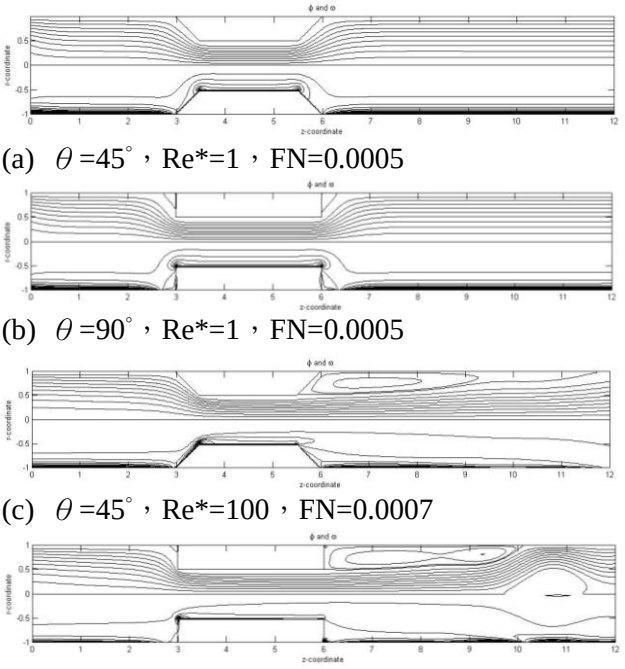

(a) θ =45°，Re*=1，FN=0.0005

(b) θ =90°，Re*=1，FN=0.0005

(c) θ =45°，Re*=100，FN=0.0007

(d) θ =90°，Re*=100，FN=0.0007

Fig. 10 Flow fields of sudden contraction/expansion tube by numerical simulation.

In the θ =45° contraction/expansion tube, for Reynold number Re*=1 and surface tension factor FN=0.0005, the recirculation zone is not obvious yet as shown in Fig. 10 (a). However, the outset of the recirculation zone is shown in Fig. 10 (b) in the θ =90° contraction/expansion tube. The maximum vorticity values in the in the θ =45° and 90° contraction/expansion tubes are 26.0712 and -29.6263, respectively.

It is conspicuous that the occurrence of recirculation zone at the corner of the sudden expansion tube by increasing Reynold number from Re*=1 till Re*=100. The maximum vorticity values in the in the θ =45° and 90° contraction/expansion tubes are -60.8587 and -82.0854, respectively.

The developments of 'lip' or 'corner' vortices on the corner are reported by Dimakopoulos repoted in 2007. The occurrence of recirculation zone and the developments of 'corner' vortices may cause the instability phenomenon shown in Fig.7(b).

3.2.2 Bubble evolution contours

Fig. 11 shows the contours of bubble penetrating through the viscoplastic fluids in the contraction/expansion tubes by numerical method.

Fig. 11 (a) and (b) show the bubble front contours in the contraction/expansion tubes with θ =45° and 90° as Re*=1，E*=0.0005，FN=0.0005 at time steps (t*): 1000, 1200, 1400, 1600, 1800, 2000, 2200, 2400, 2900, 3400, 3900, 4400 and 4900.

As the bubble front approaching the shrinking neck, the bubble front deforms into a sharper shape. The bubble reassumes its well-developed profile after fully entering the narrower tube. As the bubble front runing through the expansion throat, it increases its width and the bubble front becomes nearly parabolic shown as in Fig. 11 (a) and (b). These results are agreed with the result of Dimakopoulos et al.[9] in 2003.

However, the bubble front in the θ = 90° tube expanses more outward than that in the θ =45° tube, as the bubble front entering the expansion tube. After entering the tube, it increases its width and its front becomes again nearly parabolic, although a local minimum in thickness remains in the contraction region.

Fig. 11(c) and (d) show the bubble front contours in the contraction/expansion tubes with θ =45° and 90° as Re*=100，E*=0.0005，FN=0.0005 at time steps (t*): 200, 240, 280, 320, 360, 400, 440, 480, 580, 680, 780, 880 and 1000.

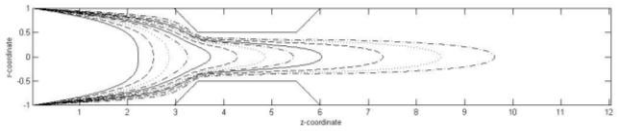

(a) θ =45°，Re*=1，FN=0.0005

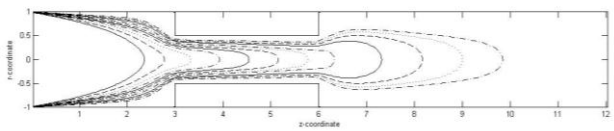

(b) θ =90°，Re*=1，FN=0.0005

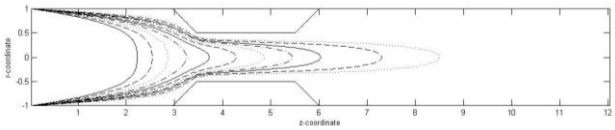

(c) θ =45°，Re*=100，FN=0.0005

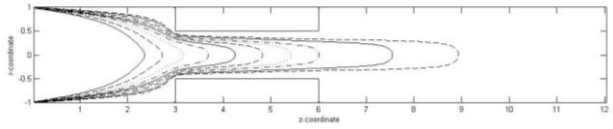

(d) θ =90°，Re*=100，FN=0.0005

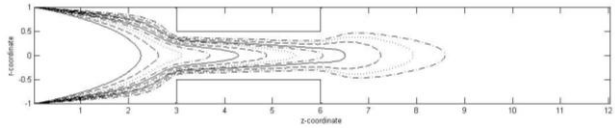

(e) θ =90°，Re*=100，FN=0.0007

Fig. 11 Bubble evolution profiles in contraction/expansion tubes by numerical method.

The effects of surface tension and inertia force on the shape of bubbles can be verified by comparing the differences of Fig. 11(d) and (e). The bubble contour changes from the fingers shape into an oval shape in the θ =90° sudden expansion tube, by increasing the factor of surface tension (FN). The only difference factor between 11(d) and (e) is the surface tension factor (FN). Therefore, the surface tension can be considered as the impact factor.

If the surface tension affects the interface of gas and fluid more significant, the bubble will expands radially, and then the bubble contour is closer to the oval. In the other hand, if the inertia force is more significant, a slender bubble profile is formed. This result is consistent with the results of the experimental observations very well.

4 Conclusion

This paper studies the behavior of a long bubble through the viscoplastic fluids filled in a contraction/expansion tube was studied experimentally and numerically.

As the bubble front approaching the shrinking neck, the bubble front deforms into a sharper shape. And then the bubble reassumes its well-developed profile after fully entering the narrower tube. As the bubble front penetrating through the expansion corner, it increases its width and the bubble front becomes nearly parabolic.

The bubble front velocity increases by increasing the contraction/expansion angle under a constant incident gas flow rate. Moreover, the bubble front velocity increases by increasing the incident gas flow. It also leads to the results including the

decreasing diameter of the bubbles as well as the increasing fractional converges of fluid.

Therefore, the bubble front shape, bubble front velocity and fractional converge of fluid changes depending on the effects of the viscosity of the fluid, the incident gas flow rate and the contraction / expansion angle.

Acknowledgement

This research was supported by the Teacher Research Support Scheme of Taoyuan Innovation of Institute Technology/ grant no. 101P-001.

References:

[1] P. G. Saffman and F. R. S. Geoffrey Taylor, The Penetration of a Fluid into a Porous Medium or Hele-Shaw Cell Containing a More Viscous Liquid, *Proceedings of the Royal Society of London. Series A, Mathematical and Physical Sciences*, vol. 245, 1958, pp. 312-329.

[2] G. I. Taylor, Deposition of a Viscous Fluid on the Wall of a Tube, *Journal of fluid mechanics*, vol. 10, 1961, pp. 161-165.

[3] E. Pitts, Penetration of gluid into a Hele-Shaw cell: The Saffman-Taylor experiment, *Journal of fluid mechanics*, vol. 97, 1980, pp. 53-64.

[4] Y. Takehiro, Three-dimensional viscoelastic flows through a rectangular channel with a cavity, *J. Non-Newtonian Fluid Mech*, vol. 114, 2003, pp. 13-31.

[5] D. A. Reinelt and P. G. Saffman, The penetration of a finger into a viscous fluid in channel and tube, *SIAM J. Sci. Stat. Comput.*, vol. 6, 1985, pp. 542-561.

[6] J. H. Song and J. Y. Yoo, Numerical Simulation of Viscoelastic Flow Through a Sudden Contraction Using a Type Dependent Difference Method, *J.Non Newtonian Fluid Mech.*, vol. 24, 1987, pp. 221-243.

[7] C. H. Hsu, P. C. Chen, K. Y. Kung, G. C. Kuo, The Gas-assisted Expelled Fluid Flow in the Front of a Long Bubble in a Channel, *WSEAS TRANSACTIONS on APPLIED and THEORETICAL MECHANICS*, Vol. 4, 2010, pp.11-21.

[8] P. C. Huzyak and K. W. Koelling, The penetration of a long bubble through a viscoelastic fluid in a tube, *Journal of Non-Newtonian Fluid Mechanics*, vol. 71, 1997, pp. 73-88.

[9] Y. Dimakopoulos and J. Tsamopoulos, Transient displacement of a viscoplastic material by air in straight and suddenly constricted tubes, *Journal of Non-Newtonian Fluid Mechanics*, vol. 112, 2003, pp. 43-75.

[10] Y. Dimakopoulos and J. Tsamopoulos, On the gas-penetration in straight tubes completely filled with a viscoelastic fluid, *Journal of Non-Newtonian Fluid Mechanics*, vol. 117, 2004, pp. 117-139.

[11] Y. Dimakopoulos and J. Tsamopoulos, Transient displacement of Newtonian and viscoplastic liquids by air in complex tubes, *Viscoplastic fluids: From theory to application*, vol. 142, 2007, pp. 162-182.

[12] M. Ohta, et al., Dynamic processes in a deformed drop rising through shear-thinning fluids, *Journal of Non-Newtonian Fluid Mechanics*, vol. 132, 2005, pp. 100-107.

[13] I. Christie, et al., Flow of a non-Newtonian fluid between eccentric rotating cylinders, *International Journal of Engineering Science*, vol. 25, 1987, pp. 1029-1047.

[14] K. R. Rajagopal, et al., A note on the falkner-skan flows of a non-newtonian fluid, *International Journal of Non-Linear Mechanics*, vol. 18, 1983, pp. 313-320.

[15] Y. Dimakopoulos and J. Tsamopoulos, Transient displacement of Newtonian and viscoplastic liquids by air in complex tubes, *Journal of Non-Newtonian Fluid Mechanics*, vol. 142, 2007, pp. 162-182.

[16] C. H. Hsu, K. Y. Kung,P. C. Chen, S. Y. Hu, THE VISUALIZATION OF GAS-ASSISTED INJECTION LONG BUBBLE IN A TUBE, *Proceedings of the 8th WSEAS International Conference on Applied Computer and Applied Computational Science*, 2011, pp.163-168.

[17] W.-Y. Dzan, H.-J. Yang, H.-C. Lin, A Research of Digitizing Ship Design and Stability Analysis, *WSEAS TRANSACTIONS on APPLIED and THEORETICAL MECHANICS*, Vol. 5, 2010, pp.11-22.

[18] D. Munger, A. Vincent, A Level Set Approach to Simulate Magnetohydrodynamic Instabilities in Aluminum Reduction Cells, *Journal of Computational Physics*, vol. 217, 2006, pp.295–311.